9.3 An Output-Domain-Independent Single-Transmitter-Dual-Receiver Wireless Power Transfer System with Detuned-Tank and Time-Multiplexing Control for Adaptive Power Distribution

Yutang Chen, Yifan Lin, Dihu Chen, Jianping Guo

Sun Yat-Sen University, Guangzhou, China

Abstract

This paper presents an output-domain-independent single-transmitter-dual-receiver wireless power transfer system. The proposed detuned-tank and time-multiplexing control enable adaptive power distribution, preventing power conflicts caused by different receiver impedance (Z_{RX}) and coupling coefficient (k). The system achieves two output domains over k ranging from 0.14 to 0.28, with excellent load regulation of 0.07/0.26mV/mA, a peak efficiency of 82.2% and a maximum output power of 1099mW.

With the growing number of portable, wearable, and implantable devices, multi-output wireless power transfer (WPT) systems have become increasingly important [1-6]. Previous solutions typically realize multiple outputs within a single receiver (RX) and cannot simultaneously deliver multiple outputs across different RX devices (i.e., cannot achieve independent output domains), which limits their application scenarios. To power multiple RXs, multi-transmitter (TX)-multi-RX systems have been proposed [7,8]. However, the use of multiple TX tanks can lead to magnetic field cancellation, resulting in higher power consumption. Clearly, a single-TX-multiple-RX WPT system provides a simple and effective solution for achieving independent output domains, as illustrated in Fig. 9.3.1 (top left).

To realize a single-TX-dual-RX (STDR) system, multi-frequency resonating compensation (MFRC) networks have been proposed in [9,10], as illustrated in Fig. 9.3.1 (top right). The MFRC creates low impedance at two frequencies: the TX resonant tank and the first RX (RX1) are tuned to the fundamental frequency ω_0, while the MFRC and the second RX (RX2) are tuned to a higher frequency ω_1 ($\geq 2\omega_0$). This allows both RXs to receive power simultaneously. However, MFRC is unsuitable for MHz-frequency WPT systems with narrow ISM bands, and switching losses increase at high frequencies. An alternative STDR-WPT system was proposed in [11], in which a rectifier followed by a DC-DC buck converter is adopted at RX to achieve voltage regulation. However, the cascaded power stage reduces overall power efficiency. Moreover, the aforementioned works [9-11] were implemented with discrete components, limiting integration.

The single-stage reconfigurable resonant regulating (R^3) rectifier [12] can significantly improve efficiency, but it introduces power conflicts in STDR-WPT systems. As shown in Fig. 9.3.1 (middle left), the 0X mode presents a low RX impedance Z_{RX}, corresponding to a high reflected impedance Z_{RL}, whereas the 1X mode exhibits the opposite behavior. Consequently, an RX operating in 0X mode absorbs most of the TX power, but this power is largely wasted in freewheeling and does not contribute to the output V_O. Conversely, the RX in 1X mode receives insufficient input power, resulting in poor load regulation, particularly under heavy-load conditions. To address this power conflict, an open-mode RX for isolated DC-DC conversion was proposed [13], which operates similarly to the R^3 rectifier in WPT systems. However, the open-mode RX cannot function in a single-RX WPT system due to the absence of a freewheeling phase. In addition, the coupling coefficient k also affects Z_{RL} and can exacerbate power conflicts. When both RXs operate in 1X mode, power is preferentially delivered to the higher-k RX, resulting in poor regulation of the RX with lower k.

In this work, a STDR-WPT system with detuned-tank control (DTC) and time-multiplexing control (TMC) is proposed to achieve adaptive power distribution, as illustrated in Fig. 9.3.1 (middle right). The proposed DTC mitigates the impact of Z_{RX} by controlling the GaN FET (EPC2012C) while retaining the freewheeling path necessary for output regulation. Meanwhile, the proposed TMC, enabled via RX-RX communication, alleviates the influence of the coupling coefficient k. As shown in Fig. 9.3.1 (bottom), the DTC introduces two detuned 0X/1X (D0X/D1X) modes, where a capacitor C_{DT} is series-connected into the LC tank to increase Z_{RX} through the added impedance Z_{DT}. Consequently, the reflected impedance Z_{RL} in the detuned mode decreases, reducing the power received by the RX. Additionally, in D0X mode, the input current continues to freewheel, ensuring correct operation in both single-and dual-RX systems. Since Z_{RL} is also affected by k, C_{DT} is chosen as half of C_{RX} to ensure a reasonable power distribution under extreme conditions. Assuming RX1 operates under the lowest coupling coefficent (k_1) and RX2 under the highest (k_2=2k_1), the Z_{RL} of RX1 in 1X mode remains higher than that of RX2 in D0X mode. In this way, a sufficiently large Z_{DT} compensates for the influence of k.

Figure 9.3.2 (left) describes the circuit implementations of the proposed RX chip, which integrates an R^3 rectifier, a current sensor, a feedback resistor chain, a GaN driver for M_N, two detectors for input current amplitude and V_O, and a controller. In the DTC, the signal V_{RM} determines whether the rectifier operates in full-bridge rectification or freewheeling, while the signal V_{DTU} turns M_N on or off to detune the LC tank. When the TMC is inactive, the RX will only switch between 1X and D0X modes. Since Z_{RL} in 1X mode is higher than in D0X mode, TX power preferentially flows to the 1X-mode RX, ensuring a reasonable power distribution.

Additionally, the TMC will be enabled via RX-RX communication when both RXs operate in 1X mode simultaneously. The workflows of the RXs are shown in Fig. 9.3.2 (right), and the operation principle of the proposed system is illustrated in Fig. 9.3.3. In period I, V_{O1} in the low-k RX1 rises in 1X mode, while V_{O2} in the high-k RX2 decreases in D0X mode. With the proposed DTC, no power conflict occurs. In period II, when RX2 transitions from D0X mode to 1X mode, TX power preferentially flows to RX2 due to its large k and high Z_{RL}, causing V_{O1} to decrease unexpectedly in 1X mode and degrading load regulation. To address this issue, the proposed RX chip employs a voltage detector to sense power conflict induced by k, with the reference voltage V_{TH1} set below the hysteresis window. In period III, once V_{O1} falls below V_{TH1}, RX-RX communication is enabled. A 2μs blanking signal V_{BLK1} is inserted into V_{RM1}, briefly forcing RX1 into 0X mode. As Z_{RL} is large in 0X mode, the input current i_{RX1} increases, while i_{RX2} in RX2 decreases. In period IV, the amplitude detector in high-k RX2 senses the reduction in i_{RX2}, thereby enabling the TMC. An 8μs clock signal V_{CLK} with 25% duty cycle is inserted into V_{DTU}. Consequently, RX2 switches between D1X and 1X modes: when RX2 is in D1X mode, most power is delivered to RX1, raising V_{O1}; when RX2 is in 1X mode, power flows to V_{O2}. The TMC thus eliminates the power conflict caused by k and ensures proper regulation for both RXs. In period V, if V_{O1} and V_{O2} reach the upper hysteresis window, both RXs enter D0X mode.

In the adopted TMC, D1X mode is chosen over D0X mode for two reasons. First, D1X mode has the lowest Z_{RL} among the four operation modes in the proposed WPT system, allowing low-k RX1 to receive high power. Second, although the input power transferred to high-k RX2 is insufficient, it can still be delivered to V_{O2}. In the clock generator, a relatively long period is preferred to suppress ringing and instability of i_{RX1} and i_{RX2} during mode switching, providing steady and sufficient power delivery. Meanwhile, a 25% duty cycle is selected to charge V_{O1} for a longer time, thereby improving the load regulation. Figure 9.3.2 (bottom) shows the proposed amplitude detector enabled by signal V_{EN}. This detector is activated under the following conditions: 1) the RX is in 1X mode (i.e., V_{HY}=1); 2) V_O is within the hysteresis window (i.e., V_{DVO}=0); and 3) the input current is sufficient (i.e., V_{AVG}>V_{TH3}, resetting V_{DIRX}). Additionally, an RC low-pass filter is incorporated to suppress narrow mis-triggered pulses generated by the input current ringing.

Figure 9.3.4 shows the measured steady-state waveforms under different load currents. In Fig. 9.3.4 (top), with 50mA I_{L1} and 165mA I_{L2}, both outputs V_{O1} and V_{O2} are properly regulated at 4V using the proposed DTC. Since their 1X modes rarely overlap, the TMC remains inactive. In Fig. 9.3.4 (middle), when I_{L1} increases to 70mA, the original duration of 1X mode becomes insufficient to support the load, causing V_{O1} to drop. When V_{O1} falls below V_{TH1}, RX-RX communication is triggered, activating the TMC in the high-k RX2. This enables adaptive power distribution and simultaneous charging of both outputs, thereby eliminating the impact of k. Figure 9.3.4 (bottom) compares the output voltages with and without the TMC, showing that the TMC significantly improves load regulation, especially under heavy-load conditions.

Figure 9.3.5 (top) shows the measured load transient response waveforms, where I_{L2} is fixed at 165mA, while I_{L1} switches between 10mA and 102mA. Both outputs maintain correct regulation, with unnoticeable voltage droop or recovery time. As depicted in Fig. 9.3.5 (bottom left), with proposed DTC and TMC, the load regulation in the low-k RX1 is significantly improved, especially under heavy load, decreasing from 1.27mV/mA to 0.07mV/mA. The power efficiency is shown in Fig. 9.3.5 (bottom right), with a peak efficiency of 82.2%, and a maximum output power of 1099mW.

Figure 9.3.6 summarizes the performance and compares it with state-of-the-art WPT systems. To the best of our knowledge, this is the first reported output-domain-independent STDR-WPT system with highly integrated RX chips, in which power conflicts caused by Z_{RX} and k in conventional topologies are eliminated, and adaptive power distribution is achieved through the proposed DTC and TMC strategies. The measurement results show that two independent output domains can be well generated, with good load regulation of 0.07/0.26 mV/mA. The measured peak efficiency is 82.2%, and the maximum output power is 1099mW. The output voltages recover instantly, with negligible voltage droop during load transients. Figure 9.3.7 shows the RX chip micrograph, occupying an area of 0.9×1.75mm^2. The TX and RX coils are designed with inductances of 2.2μH and 551nH, and parasitic resistances of approximately 620mΩ and 310mΩ, respectively. The measured k ranges from 0.28 to 0.14 as the coil distance varies from 4 to 10mm.

 979-8-3315-8936-3/26/$31.00

Acknowledgement:
This work was partly supported by the Key Area R&D Program of Guangdong Province under Grant 2022B0701180001, and the National Natural Science Foundation of China under Grant 62274189. Corresponding author: Jianping Guo.

References:

[1] J. Lin et al., "A Single-Stage Dual-Output Regulating Rectifier With Hysteretic Current-Wave Modulation," *IEEE JSSC*, vol. 56, no. 9, pp. 2770-2780, Sep. 2021. https://doi.org/10.1109/JSSC.2021.3071221

[2] Y. Chen et al., "A 2-W, 90%-Efficiency Single-Stage Dual-Output Wireless Power Receiver with 0.1 to 700-mA Output Current Range Through Dynamic Delay Compensation and Bootstrap Adaptive Body Biasing Circuit," *A-SSCC*, pp. 1-3, Nov. 2023. https://doi.org/10.1109/A-SSCC58667.2023.10348004

[3] F. Wang et al., "A Hybrid-Resonance Single-Stage Dual-Output Rectifier With High Voltage Difference for Wireless Power Transfer System," *A-SSCC*, pp. 1-3, Nov. 2024. https://doi.org/10.1109/A-SSCC60305.2024.10848581

[4] H.-S. Lee et al., "A 90.8%-Efficiency SIMO Resonant Regulating Rectifier Generating 3 Outputs in a Half Cycle with Distributed Multi-Phase Control for Wirelessly-Powered Implantable Devices," *ISSCC*, pp. 448-449, Feb. 2024. https://doi.org/10.1109/ISSCC49657.2024.10454403

[5] T. Lu and S. Du, "A 92.3%-Efficiency Switching-Mode Dual-Output Regulating Rectifier With Improved Link Adaptability for Wireless Power Transfer," *IEEE JSSC*, vol. 60, no. 7, pp. 2354-2366, Jul. 2025. https://doi.org/10.1109/JSSC.2025.3540596

[6] Q. Zhuang et al., "A 6.78MHz Single-Stage Regulating Rectifier with Dual Outputs Simultaneously Charged in a Half Cycle Achieving 92.2% Efficiency and 131mW Output Power," *ISSCC*, pp. 188-189, Feb. 2025. https://doi.org/10.1109/ISSCC49661.2025.10904779

[7] H. Qiu et al., "A 6.78-MHz Coupling Coefficient Sensorless Wireless Power Transfer System Charging Multiple Receivers With Efficiency Maximization by Adaptive Magnetic Field Distributor IC," *IEEE TCAS-I*, vol. 71, no. 2, pp. 974-983, Feb. 2024. https://doi.org/10.1109/TCSI.2023.3340681

[8] X. Wang et al., "Multioutput Wireless Charger for Drone Swarms With Reduced Switch Requirements and Independent Regulation Capability," *IEEE TIE*, vol. 71, no. 5, pp. 4883-4895, May 2024. https://doi.org/10.1109/TIE.2023.3277116

[9] Z. Zhang et al., "Multiple-Frequency Resonating Compensation for Multichannel Transmission of Wireless Power Transfer," *IEEE TPEL*, vol. 36, no. 5, pp. 5169-5180, May 2021. https://doi.org/10.1109/TPEL.2020.3027916

[10] Y. Gong et al., "Selected-Interharmonic-Injected Pulse Density Modulation for One-to-Many WPT Systems," *IEEE TPEL*, vol. 39, no. 9, pp. 11784-11793, Sep. 2024. https://doi.org/10.1109/TPEL.2024.3402209

[11] M. Fu et al., "Megahertz Multiple-Receiver Wireless Power Transfer Systems With Power Flow Management and Maximum Efficiency Point Tracking," *IEEE TMTT*, vol. 65, no. 11, pp. 4285-4293, Nov. 2017. https://doi.org/10.1109/TMTT.2017.2689747

[12] J. Ge et al., "A 6.78-MHz 79.5%-Peak-Efficiency Wireless Power Transfer System using a Wireless Mode-Recognition Technique and a Fully-On/off Class-D Power Amplifier," *ISSCC*, pp. 446-447, Feb. 2024. https://doi.org/10.1109/ISSCC49657.2024.10454467

[13] J. Jiang et al., "A Single-Link Multi-Domain-Output (SLiMDO) Isolated DC-DC Converter with Passive Magnetic Flux Sharing for Local Energy Distribution and Rx Behavior Sensing-Based Global Power Modulation," *ISSCC*, pp. 530-531, Feb. 2025. https://doi.org/10.1109/ISSCC49661.2025.10904792

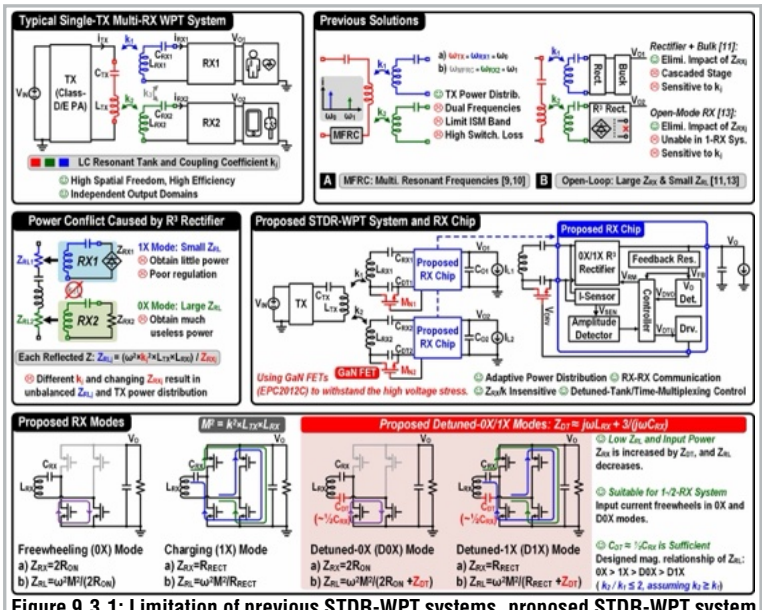

Figure 9.3.1: Limitation of previous STDR-WPT systems, proposed STDR-WPT system with detuned-tank and time-multiplexing control, and proposed RX modes.

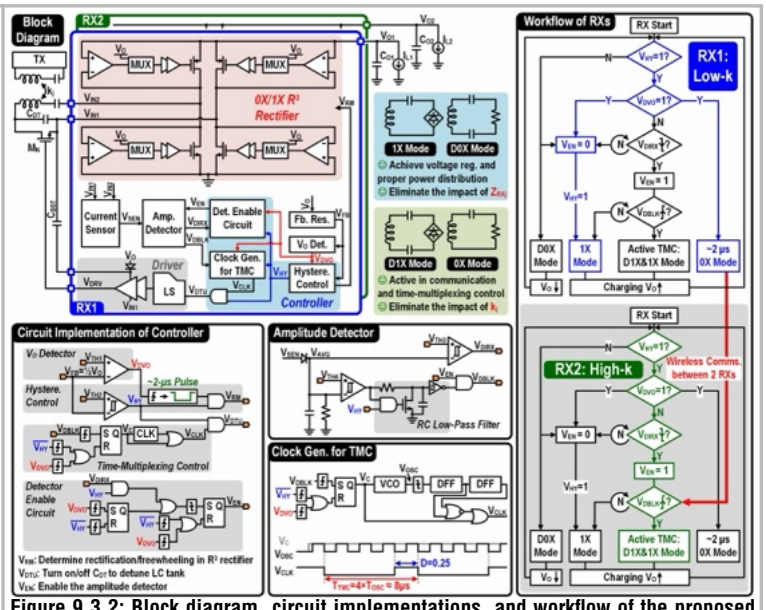

Figure 9.3.2: Block diagram, circuit implementations, and workflow of the proposed RX chip for the STDR-WPT system.

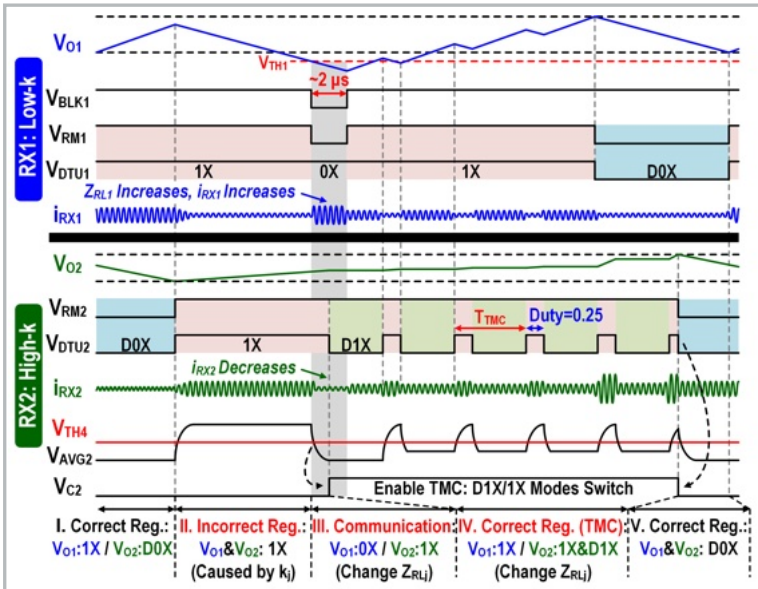

Figure 9.3.3: Timing diagram and operation principle of the proposed STDR-WPT system, illustrated under a low-k RX1 and high-k RX2 condition.

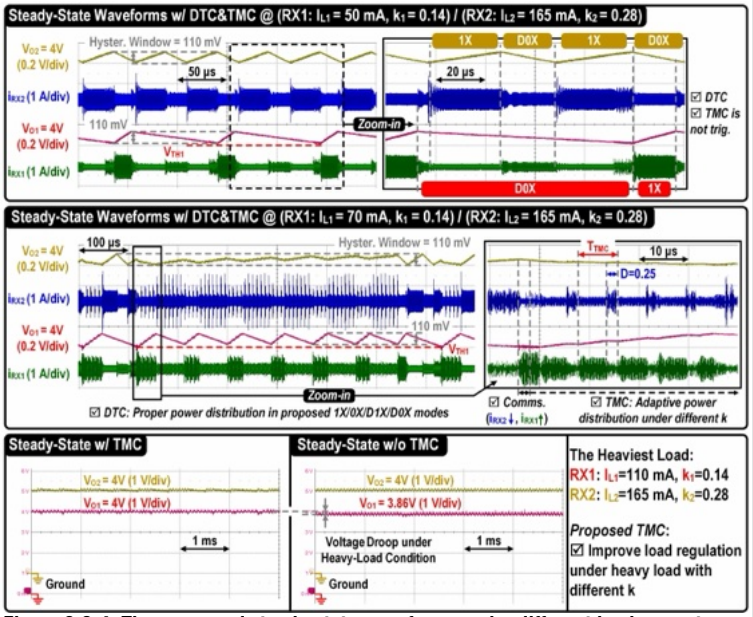

Figure 9.3.4: The measured steady-state waveforms under different load currents.

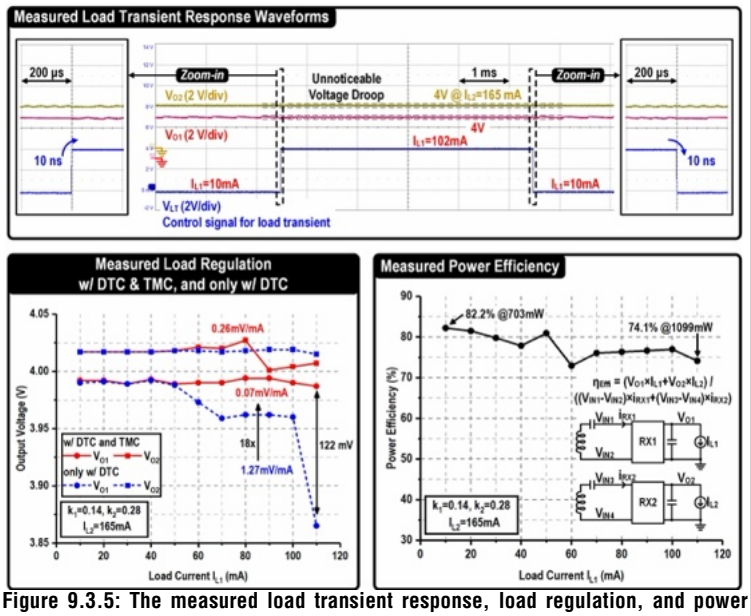

Figure 9.3.5: The measured load transient response, load regulation, and power efficiency.

	[1] JSSC 2021	[4] ISSCC 2024	[5] JSSC 2025	[6] ISSCC 2025	This work
Technology	180nm CMOS	250nm CMOS	180nm CMOS	180nm CMOS	180nm CMOS
RX Tank	Series	Parallel	Parallel	Parallel	Series
RX Structure	SSDO R^3 Rectifier	SIMO R^3 Rectifier	Dual-Output Voltage Doubler	SSDO R^3 Rectifier	Detuned R^3 Rectifier
Frequency (MHz)	6.78	2	6.78	6.78	6.78
# of Outputs	2	3	2	2	2
Independent Output Domains	1	1	1	1	2
RX-RX Comms.?	No	No	No	No	Yes
Adaptive Power Distribution	None	None	None	None	Detuned-Tank/ Time-Multiplexing Ctrl.
V_O (V)	1.8/3.3	1-4.5	1.8/3.3	1-3.3	4
Max. P_O (mW)	1020	135.53	171	131	1099
Trans. V_O Droop	Unnoticeable	N/A	Unnoticeable	Unnoticeable	Unnoticeable
Recovery Time	Instant	N/A	Instant	Instant	Instant
Load Reg. (mV/mA)	0.23	N/A	N/A	N/A	0.07/0.26
Peak Efficiency (%)	91.9	90.82	92.3	92.2	82.2
Range of k	N/A	N/A	N/A	N/A	0.14-0.28

Figure 9.3.6: Performance summary and comparison with the state-of-the-art WPT systems.

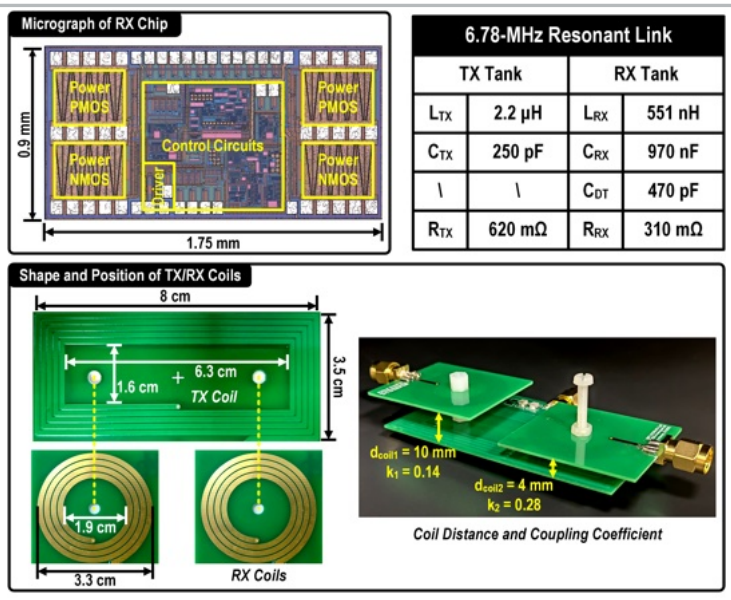

Figure 9.3.7: Die micrograph of RX chip, and information of TX/RX tanks.

979-8-3315-8936-3/26/$31.00